Inferring the Dynamics of Ionic Currents from Recursive Piecewise Data Assimilation of Approximate Neuron Models

Stephen A. Wells, Joseph D. Taylor, Paul G. Morris,* and Alain Nogaret†

Department of Physics, University of Bath, Bath BA2 7AY, United Kingdom

We construct neuron models from data by transferring information from an observed time series to the state variables and parameters of Hodgkin-Huxley models. When the learning period completes, the model will predict additional observations and its parameters uniquely characterize the complement of ion channels. However, the assimilation of biological data, as opposed to model data, is complicated by the lack of knowledge of the true neuron equations. Reliance on guessed conductance models is plagued with multivalued parameter solutions. Here, we report on the distributions of parameters and currents predicted with intentionally erroneous models, overspecified models, and an approximate model fitting hippocampal neuron data. We introduce a recursive piecewise data assimilation algorithm that converges with near-perfect reliability when the model is known. When the model is unknown, we show model error introduces correlations between certain parameters. The ionic current waveforms reconstructed from these parameters are excellent predictors of true currents and carry a higher degree of confidence, greater than 95.5%, than underlying parameters, which is 53%. Unexpressed ionic currents are correctly filtered out even in the presence of mild model error. When the model is unknown, the covariance eigenvalues of parameter estimates are found to be a good gauge of model error. Our results suggest that biological information may be retrieved from data by focusing on current estimates rather than parameters.

I. INTRODUCTION

Data assimilation is a first-in-class method for building models of nonlinear dynamical systems [1–6]. It estimates parameters by synchronizing the model state variables to time series observations. Once the training period is complete, the optimized models successfully predict complex time series oscillations ranging from chaotic dynamics [7,8] to biological neurons [9–12] and networks [13]. The estimated parameters hold the further promise of revealing hidden internal properties of biological systems. The challenge, however, is that the state equations of neurons are generally unknown and modeling neurons with empirical models such as the Hodgkin-Huxley model [9,10,14–19] introduces model error which biases parameter estimates away from true values [20–28]. Although much attention has been paid to multivalued parameter solutions in biological inference problems [29–32], a systematic study is needed to understand its pervasiveness in the optimization of *erroneous nonlinear models* which goes beyond the biological argument

that redundant parameters are needed to preserve a capacity to adapt [31,32]. Correcting parameter sloppiness is complicated by additional requirements that the optimization problem has to meet such as observability [33–36] (the state vector is uniquely constrained at every point of the assimilation window) and identifiability [8,37–42] (the stimulation protocol elicits enough information from the neuron to constrain all model parameters). These conditions can be difficult to quantify and are not systematically checked [9,43–47]. As a result, several authors have opted to develop leaner models with fewer parameters [48–50] in an attempt to reduce parameter error or simply focused on predictions alone [29].

Here, we show that the currents passing through ion channels can be predicted more reliably than ion channel parameters. We propose that the covariance matrix of parameter estimates constitutes a suitable metric of model error when the biological model is unknown. We introduce recursive piecewise data assimilation (RPDA) as a novel parameter search algorithm with improved convergence. Recursive piecewise data assimilation biases the state vector towards the true solution by reinjecting membrane voltage data in the state vector at regular intervals across the assimilation window. When the model is known, RPDA obtains the true solution with near perfect reliability and minimal error (less than 0.1%), independently of the choice of initial state vectors and stimulation protocols. The uniqueness of solutions proves that the observability and identifiability criteria are fulfilled. We then introduce model error by detuning the exponent of a gate variable in the Hodgkin-Huxley model and study the dispersion of parameters estimated by two erroneous variants

---

*Present address: Department of Physiology, Development and Neuroscience, University of Cambridge, Cambridge CB2 3DY, United Kingdom.

†A.R.Nogaret@bath.ac.uk

of this model (ErrM1 and ErrM2). Two further model variants adding a supplementary ion channel to the original model (ErrM3) and to its ErrM1 variant (ErrM4) gave the parameter and current dispersions of overspecified models. We find that model error introduces correlations between blocks of parameters defining the same ion channel type. The calculation of ionic currents integrates these correlations with the effect that mean current predictions deviate by less than 8% from their true values compared to over 100% for some parameters. Uncertainty on current estimates is less than 4.5%, whereas it is 47% on parameters. Overspecifying conductance models by adding extra ion channels to them is not found to induce significant compensation between parameters. Unexpressed ion channels are correctly filtered out, while those present are assigned the correct current values, even by the mildly erroneous model ErrM4. We finally compare the uncertainty on currents estimated with intentionally erroneous models (ErrM1 to ErrM4) to those of a guessed CA1 model trained on CA1 hippocampal neuron data. We find that the uncertainty on the reconstructed CA1 currents is 14% compared to 4.5% on ErrM2 currents. As the uncertainty on ionic currents increases with model error, we estimate that the error in the CA1 model is about 3 times greater than the error introduced by detuning a single gate exponent in ErrM2. Our findings suggest that the predictive accuracy of RPDA is sufficient to detect ion channel dysfunction [23,51–58] and to infer the blocking action of ion channel antagonists [59].

II. RECURSIVE PIECEWISE DATA ASSIMILATION

We use data assimilation [1,2] to optimize the state variables and parameters of Hodgkin-Huxley-type models [60] by minimizing a least-squares cost function [9,10,19]. This function measures the misfit between a state variable representing the membrane voltage x_1 and the experimental membrane voltage V_{mem} recorded at discrete times t_i, $i \in [0, N]$ spanning the assimilation window of duration T:

$$c(\vec{x}(0)) = \frac{1}{2} \sum_{i=0}^{N} \{[x_1(t_i, \vec{x}(0)) - V_{\text{mem}}(t_i)]^2 + x_{L+1}(t_i)^2\}. \quad (1)$$

The state of the neuron is represented by a vector $\vec{x}$ with $L + K + 2$ components. Vector components are x_1, the membrane voltage; $x_2, \ldots, x_L$, the gate variables of ion channels; x_{L+1} and x_{L+2}, the Tikhonov regularization variable [61–63] and its time derivative; and $x_{L+2}, \ldots, x_{L+K+2}$, the model parameters. Model parameters are treated as state variables whose time derivative is zero. If a parameter were believed to change in time, as is sometimes the case in biology, the problem formulation would easily account for this by replacing zero with the rate of change of the parameter. The cost function is minimized subject to both equality constraints

$$\frac{dx_l}{dt} = F_l(x_1, \ldots, x_{L+K+2}), \quad l = 1, \ldots, L + K + 2, \quad (2)$$

specified by the neuron model and the zero time derivatives of model parameters expressed as

$$F_l(\vec{x}) = \begin{cases} -J/C - x_{L+1}(x_1 - V_{\text{mem}}), & l = 1 \\ (x_{l\infty} - x_l)/\tau_l, & l = 2, \ldots, L \\ x_{L+2}, & l = L + 1 \\ \text{unspecified}, & l = L + 2 \\ 0, & l = L + 3, \ldots, L + K + 2 \end{cases} \quad (3)$$

and inequality constraints

$$x_l^{\min} \leqslant x_l \leqslant x_l^{\max}, \quad l = 1, \ldots, L + K + 2, \quad (4)$$

specifying the range of variation of membrane voltage, gate variables, regularization term, and parameters

$$\left[x_l^{\min}, x_l^{\max}\right] = \begin{cases} -100 \text{ mV}, 50 \text{ mV} & l = 1 \\ 0, 1 & l = 2, \ldots, L \\ 0, 1 & l = L + 1 \\ -1, 1 & l = L + 2 \\ p_l^{\min}, p_l^{\max} & l = L + 3, \ldots, L + K + 2. \end{cases} \quad (5)$$

The $J = J_{\text{Na}} + J_K + \cdots - J_{\text{inj}}$ is the current per unit area of the neuron membrane. This includes all voltage-gated ionic currents (Na, K, etc.) and the current injected to drive neuron oscillations, J_{inj}. The slow pump and exchange currents maintaining ionic gradients across the membrane are implicitly included in the constant reversal potentials E_{Na} and E_K of Na^+ and K^+ ions. The C is the membrane capacitance, τ_l is the recovery time of ionic gate l, and $x_{l\infty}$ is the steady-state value of gate variable x_l. The user sets the parameter search range $[p_l^{\min}, p_l^{\max}]$ to the widest biologically plausible range for each parameter. Data assimilation outputs the optimal parameters and the state variables at $t = 0$ as $\vec{x}(0)$.

The convergence of data assimilation is compromised by badly conditioned problems that one encounters in biology. When the model is known, the global minimum of Eq. (1) is well defined. However, systems with a large number of unobserved state variables ($L > 12$) may fail the observability criterion. This may cause the parameter search to get stuck in local minima of the cost function. These issues have been partially remedied by increasing the embedding space [8,34–36,42,64], improving the design of the injected current waveform, or using noise regularization [16,65]. These methods did not achieve 100% convergence however. When the model is unknown, as is always the case of real neurons, the global
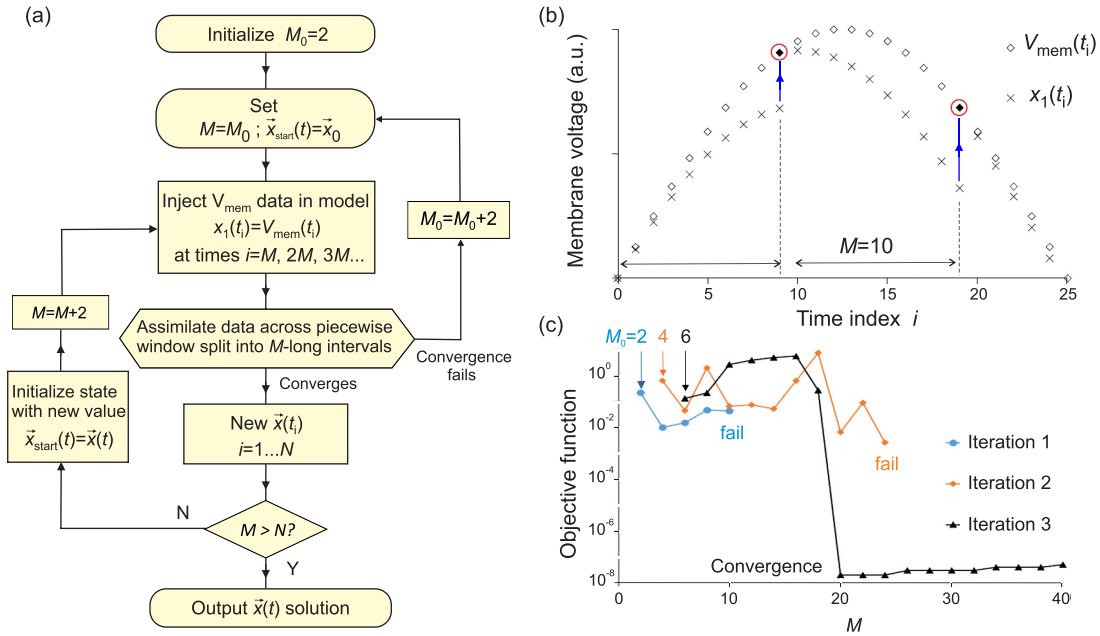
FIG. 1. RPDA algorithm. (a) Algorithm flowchart. (b) The RPDA algorithm synchronizes the membrane voltage variable x_1 to the time series data V_{mem} in blocks of M discrete time points. The algorithm reinjects V_{mem} in the model at the beginning of each block (red circle). (c) Example of recursive convergence starting from $M_0 = 6$ and increasing the block size to $M = N$. This follows two "false starts" at $M_0 = 2$ and $M_0 = 4$.

minimum may not coincide with the true solution. Parameter searches starting from different initial state vectors may get stuck at different minima, giving multivalued solutions.

The RPDA algorithm, which we present in Fig. 1(a), improves the convergence of the parameter search by applying a bias towards the true solution. This is achieved by reinjecting membrane voltage data in the optimization problem every M data points. The membrane voltage state variable x_1 is replaced with V_{mem} at time points $t_0, t_{M-1}, t_{2M-1}, \ldots$ in the expression of the equality constraints linearized by Simpson's and Hermite interpolation [65]

$$x_l(t_{i+2}) = x_l(t_i) + \Delta t \left(\frac{1}{3} F_l(\vec{x}(t_i)) + \frac{4}{3} F_l(\vec{x}(t_{i+1})) \right.$$

$$\left. + \frac{1}{3} F_l(\vec{x}(t_{i+2})) \right),$$

$$x_l(t_{i+1}) = \frac{1}{2}[x_l(t_i) + x_l(t_{i+2})] + \frac{\Delta t}{4}[F_l(\vec{x}(t_i)) - F(\vec{x}(t_{i+2}))],$$

$$l = 1, \ldots, L + K + 2, \quad i = 0, \ldots, N - 2, \quad (6)$$

where $\Delta t = T/N$. At other times the state vector is propagated normally from t_i to t_{i+2} by Eqs. (6). The substitution of V_{mem} also impacts the first and second derivatives of the objective function with respect to x_1. Where the cost function ceases to depend on x_1, its derivatives with respect to x_1 vanish. We explicitly set these derivatives to zero at times $t_0, t_{M-1}, t_{2M-1}, \ldots$. This produces a discontinuity in $x_1(t)$ at the beginning of each M block [Fig. 1(b)], which is the trade-off for imposing the bias to the solution. Our piecewise fit of data has similarities to the multiple shooting approach proposed by Zimmer and co-workers [3,66]. However, our RPDA

method performs piecewise assimilation of blocks of data through *redefined constraints*, whereas Zimmer and Sahle's approach *redefines the cost function*.

The RPDA algorithm recursively improves the accuracy of parameter estimates by relaxing the bias and reinjecting data over longer M intervals while restarting the parameter search from the previous estimate. The initial block size is $M_0 = 2$. The estimated state vector is then used as the new initial state in the next parameter search when M is incremented from M_0 to $M_0 + 2$. The search terminates when M becomes greater than N ($N = 50\,001$). The iterations ultimately restore the continuity of $x_1(t)$ across the assimilation window. When the initial bias is too strong the parameter search may fail. The algorithm then restarts the parameter search from the next larger block size ($M_0 = 4$). This process is depicted in Fig. 1(c), where the parameter search is restarted twice after convergence failed starting from $M_0 = 2$ and then $M_0 = 4$ to succeed with $M_0 = 6$.

Previous work [16,65] has explored the use of additive noise as a regularization method, showing that the stochastic perturbation of the fitting landscape by noise can disrupt local minima and improve convergence to the global minimum. In the RPDA method, each segment of length M similarly perturbs the fitting landscape. However, this perturbation will be different for each value of M. Thus, if the minimization stops at a (false) local minimum solution with one segment length, it will be driven away from this minimum when the next segment length is used. With each iteration, the solution remains a good solution due to the bias from reinjected data. As the segment length increases, minima become deeper and narrower [67] until the bias vanishes at $M = N$ and the true solution is obtained.
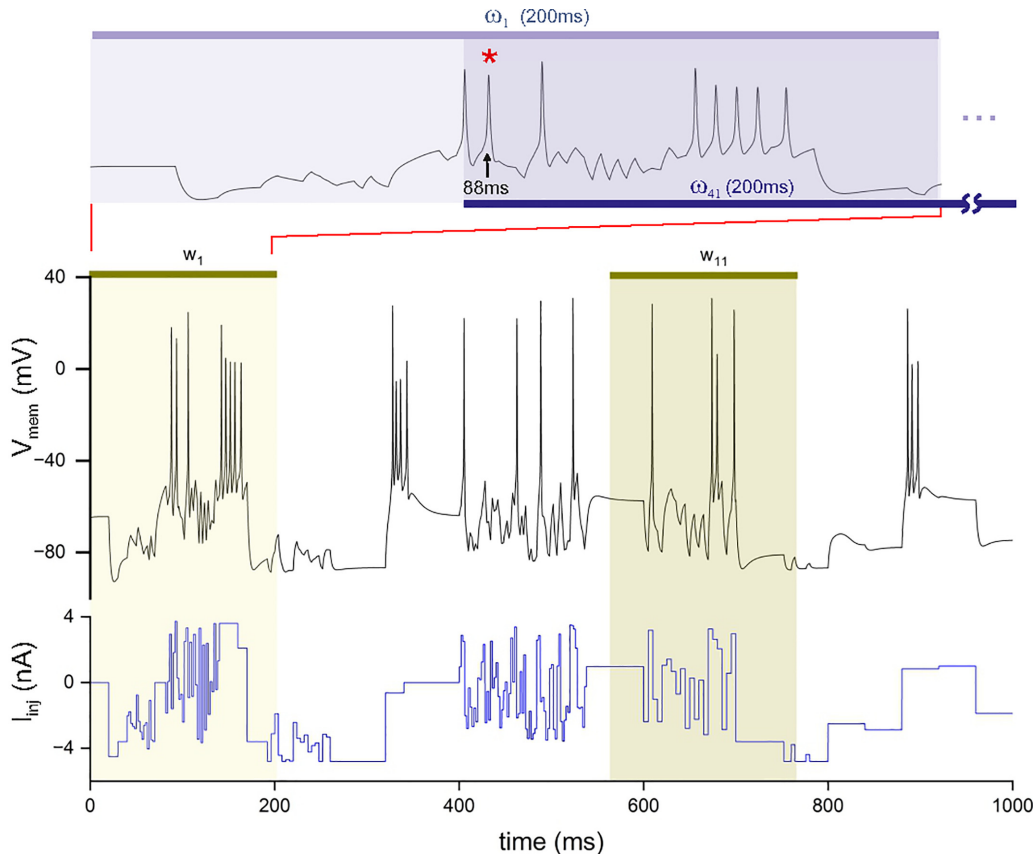
FIG. 2. Neuron oscillations and assimilation ranges. Membrane voltage (black trace) is generated by forward integration of the injected current protocol (blue trace) with the original RVLM model. The $w_1, \ldots, w_{11}$ are the 11 assimilation windows used to generate the data in Table I from well-posed problems. Each window is 200 ms wide (yellow bands) and offset from the next by 40 ms. The top panel shows the 41 assimilation windows $\omega_1, \ldots, \omega_{41}$ used to the generate the data in Table II from ill-posed problems. These windows are also 200 ms long but offset by 2 ms so that all encompass the same action potential labeled by an asterisk at 88 ms.

III. RESULTS

We then examined the accuracy of RPDA in three cases of model error in the assimilating model: (i) The model is known and is correct, (ii) the model is erroneous but error is known, and (iii) the model is erroneous and the error is unknown. In the first case RPDA converges 100% of the time towards to the true solution. In the second case, we assimilate the same data with four variants of the original model incorporating either an erroneous gate exponent or redundant ion channels, or a combination of both. In the third case, we use a guessed conductance model to assimilate membrane voltage recordings of hippocampal neurons.

A. Well-posed problems

Our reference model is a single-compartment model of the rostral ventrolateral medulla (RVLM). This model is an exemplar of the models used to predict neuron oscillations [9,10] and is easily extended to multicompartment models. It comprises five common types of ion channels: transient sodium (NaT), delayed-rectifier potassium (K), low-threshold calcium (CaT), hyperpolarized cyclic nucleotide (HCN), and leak (Appendix A). The model has $L = 7$ state variables and $K = 40$ adjustable parameters whose reference values

p_k $[k = l - (L + 2)]$ are listed in Table I. The RVLM model configured with these parameters was used to forward-integrate the current protocol $I_{\text{inj}}(t)$ in Fig. 2 and generate voltage oscillations $V_{\text{mem}}(t)$ over 1000 ms. The sequence of depolarizing and hyperpolarizing steps of varying amplitudes and durations was designed to elicit a response from all ionic currents in the neuron.

1. Uniqueness of solutions

The convergence of RPDA was probed by initializing the state vector $\vec{x}$ at 28 different locations: 18 initial parameter values were chosen at random in the parameter search range; the other 10 had parameters set every 1/10 of the search interval. In this way, the initial state vectors mapped the entire parameter space, allowing the parameter search to approach the solution from different directions. All assimilation runs used the same 200-ms-long data set labeled w_1 in Fig. 2.

Recursive piecewise data assimilation successfully converged to the true solution from all 28 initial conditions (100% convergence rate). Of these assimilation runs 23 converged from $M_0 = 2$. Three more required one restart from $M_0 = 4$. The last two required two consecutive restarts from $M_0 = 4$ and 6, as shown in Fig. 1(c). The mean block

TABLE I. Dispersion of parameters estimated from different initial guesses and different assimilation windows. The p_k are the true parameters used to construct the data being assimilated (Fig. 2). The μ_k and σ_k are the mean values and standard deviations of parameters estimated from different initial guesses of the state vector and assimilation window w_1. The μ'_k and σ'_k are the mean values and standard deviations of parameters estimated from assimilation windows $w_1, \ldots, w_{11}$ starting from the same state vector. Deviations from mean greater than 1% are highlighted in bold. We set $k = l - L - 2$.

		True	28 initial guesses			11 assimilation windows		
k	Parameter	p_k	μ_k	$\left|\frac{\mu_k - p_k}{p_k}\right|$ (%)	$\left|\frac{\sigma_k}{\mu_k}\right|$ (%)	μ'_k	$\left|\frac{\mu'_k - p_k}{p_k}\right|$ (%)	$\left|\frac{\sigma'_k}{\mu'_k}\right|$ (%)
1	A ($\times 0.1$ mm^2)	0.290	0.290	0.001	0.0001	0.290	0.0030	0.0050
2	g_L (mS cm^{-2})	0.465	0.465	0.002	0.0008	0.465	0.0073	0.0143
3	E_L (mV)	-65.00	-64.99	0.0009	0.0001	-65.00	0.0011	0.0045
4	g_{Na} (mS cm^{-2})	69.00	68.91	0.1310	0.0013	69.16	0.2254	0.8875
5	E_{Na} (mV)	41.00	41.01	0.0135	0.0001	40.99	0.0069	0.0200
6	V_{t2} (mV)	-39.92	-39.92	0.0025	0.0002	-39.92	0.0017	0.0082
7	δV_2 (mV)	10.00	10.00	0.0039	0.0002	9.99	0.0072	0.0293
8	$\delta V_{\tau 2}$ (mV)	23.39	23.38	0.0286	0.0009	23.39	0.0187	0.0260
9	t_2 (ms)	0.143	0.143	0.1370	0.0023	0.143	0.0731	0.1797
10	ϵ_2 (ms)	1.099	1.099	0.0066	0.0003	1.099	0.0156	0.0382
11	V_{t3} (mV)	-65.37	-65.36	0.0095	0.0003	-65.40	0.0411	0.1285
12	δV_3 (mV)	-17.65	-17.65	0.0124	0.0009	-17.65	0.0187	0.0461
13	$\delta V_{\tau 3}$ (mV)	27.22	27.21	0.0148	0.0011	27.23	0.0202	0.0807
14	t_3 (ms)	0.701	0.701	0.0624	0.0007	0.701	0.0072	0.0662
15	ϵ_3 (ms)	12.90	12.90	0.0174	0.0002	12.91	0.0906	0.2980
16	g_K (mS cm^{-2})	6.90	6.91	0.0878	0.0080	6.90	0.0293	0.1265
17	E_K (mV)	-100.00	-100.00	0.0029	0.0003	-100.01	0.0066	0.0254
18	V_{t4} (mV)	-34.58	-34.57	0.0140	0.0012	-34.58	0.0127	0.0106
19	δV_4 (mV)	22.17	22.18	0.0462	0.0027	22.18	0.0267	0.0210
20	$\delta V_{\tau 4}$ (mV)	23.58	23.59	0.0241	0.0011	23.57	0.0307	0.0560
21	t_4 (ms)	1.291	1.292	0.0491	0.0051	1.291	0.0343	0.0650
22	ϵ_4 (ms)	4.314	4.312	0.0524	0.0036	4.315	0.0269	0.1059
23	g_H (mS cm^{-2})	0.150	0.150	0.0348	0.0051	0.150	0.0455	0.1587
24	E_H (mV)	-43.00	-42.96	0.0861	0.0041	-42.99	0.0329	0.0791
25	V_{t5} (mV)	-76.00	-76.00	0.0006	0.0002	-76.02	0.0220	0.0242
26	δV_5 (mV)	-5.500	-5.517	0.3099	0.0062	-5.52	0.3440	0.5542
27	$\delta V_{\tau 5}$ (mV)	20.27	20.28	0.0338	0.0016	20.26	0.0306	**1.960**
28	t_5 (ms)	6.310	6.336	0.4088	0.0169	6.59	4.506	**17.20**
29	ϵ_5 (ms)	55.05	55.03	0.0384	0.0013	54.67	0.6879	**1.877**
30	$\bar{p}$ (μm s^{-1})	0.1034	0.1030	0.3674	0.4924	0.1030	0.7145	**5.115**
31	V_{t6} (mV)	-65.50	-65.49	0.0120	0.0006	-65.49	0.0109	0.0154
32	δV_6 (mV)	12.40	12.39	0.0798	0.0032	12.41	0.0686	0.2568
33	$\delta V_{\tau 6}$ (mV)	27.00	27.12	0.4613	0.0170	27.04	0.1503	0.3330
34	t_6 (ms)	0.719	0.738	0.5071	0.1098	0.735	2.262	**8.131**
35	ϵ_6 (ms)	13.05	13.06	0.0834	0.0072	13.03	0.1554	0.5307
36	V_{t7} (mV)	-86.00	-86.00	0.0033	0.0298	-85.98	0.0269	0.2461
37	δV_7 (mV)	-8.060	-8.064	0.0436	0.0378	-8.069	0.1164	0.2184
38	$\delta V_{\tau 7}$ (mV)	16.71	16.76	0.3021	0.0041	16.67	0.2465	**1.311**
39	t_7 (ms)	28.17	28.12	0.1802	0.0014	28.21	0.1389	**1.366**
40	ϵ_7 (ms)	288.7	286.8	0.6526	0.2672	287.0	0.5688	**2.347**

size at which the parameter search arrived within 0.1% of true values was $\langle M \rangle = 22$. This shows convergence is rapid once the algorithm has selected a suitable starting block size M_0.

The mean values of parameter estimates μ_k and their standard deviations σ_k were calculated over the 28 sets (Table I). A majority of μ_k (34/40) are within less than 0.1% of the true parameter values. Outliers such as t_3, t_5, t_7, and ϵ_7 relate to gate recovery times. This is unsurprising as the inverse recovery time is proportional to the rate of change of its gate

variable. They nonetheless remain within 1% of the true values. In general, the ultranarrow dispersions ($\sigma_k / \mu_k < 0.01\%$) confirm that parameters are fully constrained and the system is observable.

With a 100% convergence rate, the RPDA method improves over data assimilation and data assimilation with noise regularization, which achieve 67% and 94% convergence rates, respectively [65]. We next demonstrate that the current protocol fulfills the identifiability criterion by sampling different data sets.

2. Identifiability

Identifiability was investigated by probing the dispersion of parameters estimated from 11 different sections of the stimulation protocol. These are the time windows labeled $w_1, \ldots, w_{11}$ in Fig. 2. Each window is 200 ms long (10 001 data points) starting at 0, 40, 80, ..., 400 ms. The vector components of the initial state vector were set at the midpoint of the search range in all assimilation runs.

Recursive piecewise data assimilation converged in all 11 assimilation windows. The mean values of parameter estimates μ'_k and standard deviations σ'_k are shown in Table I. Most parameters are very well constrained with 31/40 showing deviations of μ'_k from true values of less than 0.1%. Unsurprisingly, parameters related to gate kinetics show the largest standard deviations. Yet the deviations of their mean values remain small, suggesting parameters retain good predictive power. For example, the standard deviations on t_6 and t_5 are 8.1% and 17%, respectively, whereas the deviations of mean predicted values from true values are 2.2% and 4.5%. Closer examination of the 11 parameter sets shows that the greater deviations occur in time windows which happen to include fewer action potentials, such as the 180–300-ms interval in Fig. 2. Excluding these windows, the standard deviations fall in the normal range reported in the previous section. This underlines the importance of including a minimum of five to six action potentials in the assimilation window for the identifiability condition to hold. Recursive piecewise data assimilation easily handles sparse actions potentials by assimilating wider time windows up to 1000 ms long (50 000 data points) and beyond using an adaptive step size [65].

For the identifiability criterion to hold, it is critical that the stimulation protocol is sufficiently informative. Had we chosen to stimulate the RVLM neuron with a constant current instead of the complex current protocol of Fig. 2, the periodic voltage oscillations induced by this current would not contain enough information to constrain all 40 parameters. Some of these parameters would hit interval boundaries [Eq. (5)] during assimilation despite the model fitting the data perfectly. The tonically stimulated neuron would be nonidentifiable and could be described as having redundant parameters or functionally overlapping parameters [31,32]. Identifiability is always conditional to the system being sufficiently stimulated. Even in large adaptive systems such as central pattern generators, changes in dynamics driven by increases in temperature [68] or pH [69,70] partially lift the functional overlap of parameters relative to the resting state. By stimulating our RVLM neuron with a complex current protocol designed to probe the hyperpolarization, subthreshold, and depolarization regimes on multiple timescales, we have elicited membrane voltage oscillations that are different for different parameter values. As a result, all 40 parameters are now uniquely constrained by the data as demonstrated by Table I. Having taken great care to demonstrate identifiability, we can now omit sloppiness associated with parameter redundancy from our argument in the rest of this paper.

3. Size of the data set

We have carried out assimilations using RPDA over larger windows of 20 001, 30 001, 40 001, and 49 999 points,

keeping the 0.02-ms time step constant. We found that the well-posed model converges in all of these cases. The accuracy of parameter estimates is very similar to the accuracy reported in Table I. This suggests that larger windows do not produce further gains in accuracy in well-posed problems once they include a minimum of approximately five action potentials.

B. Ill-posed problems

We now study the dispersion of parameters inferred by four variants of the RVLM model which keep parametrization the same. The ErrM1 variant had an erroneous gate exponent in the equation of the sodium current J_{NaT} [Eq. (A2)] where the gate probability $x_2^3 x_3$ was replaced with $x_2^2 x_3$. The ErrM2 variant increased this error further by replacing $x_2^3 x_3$ with $x_2 x_3$. The ErrM3 variant was an overspecified RVLM model with an extra potassium A channel. The ErrM4 variant combined model error with overspecification by adding the extra A channel to the ErrM1 model. Assimilating data with overspecified models was useful to determine the degree to which RPDA was able to filter out an unexpressed ion channel. A hypothesis which we will be testing here is whether RPDA assigns a finite conductance to the A channel to compensate for model error in the Na gate probability or whether RPDA succeeds in disentangling the contributions of each ion channel *in spite of* model error.

For each erroneous model, we estimated 41 sets of parameters from 41 assimilation windows $\omega_1, \ldots, \omega_{41}$ in Fig. 2. We then calculated the mean values and standard deviations of the ErrM1 and ErrM2 parameters which we compared to the true parameter values of the RVLM model (Table II). The covariance matrices of the RVLM, ErrM1, and ErrM2 parameters are plotted in Fig. 3. These show the emergence of parameter correlations as soon as model error is switched on in ErrM1 and ErrM2. We then completed the ErrM1 to ErrM4 models with the parameters estimated by RPDA and forward integrated these models to predict the Na, K, HCN, and A-type current waveforms (Fig. 4). These were compared to the true waveforms of the original RVLM model (dashed lines) to determine the error in the currents predicted by erroneous models. The degree of confidence on predictions was determined by computing the minimum and maximum current waveforms (Fig. 4) and the standard deviations on the integral charge under these curves (Table III). The Na, K, and A-type current waveforms were reconstructed at the site of one and the same action potential (labeled by an asterisk in Fig. 2), which was chosen for being common to all 41 assimilation windows used to generate the statistical sample of parameters. This choice is mainly for consistency as the current waveforms reconstructed at the site of other action potentials present a similar aspect. This is because once the current initiates neuron depolarization, the positive feedback dynamics of the Na and K currents is largely controlled by internal neuron parameters and not so much by subsequent stimulation.

1. Erroneous model variants: ErrM1 and ErrM2

Detuning the gate exponent from $x_2^3 x_3$ (RVLM) to $x_2^2 x_3$ (ErrM1) and $x_2 x_3$ (ErrM2) introduces correlations between

TABLE II. Dispersion of parameters inferred from erroneous models ErrM1 and ErrM2. The μ_k and σ_k are the mean values and standard deviations of parameters estimated from windows $\omega_1, \ldots, \omega_{41}$ using the RVLM model (reference estimates). The μ_{1k} and σ_{1k}, and μ_{2k} and σ_{2k} are the means and standard deviations of parameters estimated with the erroneous models ErrM1 and ErrM2, respectively. Figures in bold (bold and italics) single out deviations from mean greater than 1% (10%).

| | | Well-posed RVLM | | Ill-posed | | | |
| | | | | ErrM1 | | ErrM2 | |
k	Parameter	μ_k	$\left\lvert\frac{\sigma_k}{\mu_k}\right\rvert$ (%)	μ_{1k}	$\left\lvert\frac{\sigma_{1k}}{\mu_{1k}}\right\rvert$ (%)	μ_{2k}	$\left\lvert\frac{\sigma_{2k}}{\mu_{2k}}\right\rvert$ (%)
1	A ($\times 0.1$ mm^2)	0.290	0.0038	0.291	0.1325	0.293	0.2814
2	g_L (mS cm^{-2})	0.465	0.0107	0.4679	0.1104	0.4712	0.2812
3	E_L (mV)	-65.00	0.0353	-65.26	0.3737	-65.83	**1.213**
4	g_{Na} (mS cm^{-2})	69.01	0.3138	40.68	**2.794**	19.21	**1.260**
5	E_{Na} (mV)	41.00	0.0155	46.07	**1.535**	60.00	0.00
6	V_{t2} (mV)	-39.92	0.0033	-37.81	0.1669	-35.20	0.3431
7	δV_2 (mV)	9.998	0.0021	8.090	0.0476	5.256	0.0778
8	$\delta V_{\tau 2}$ (mV)	23.38	0.0041	20.76	0.1424	15.99	0.2437
9	t_2 (ms)	0.1429	0.0203	0.0920	**1.681**	0.0257	0.0425
10	ϵ_2 (ms)	1.099	0.0003	1.204	0.0107	1.357	0.0285
11	V_{t3} (mV)	-65.38	0.0542	-63.31	0.7557	-62.20	**2.037**
12	δV_3 (mV)	-17.65	0.0068	-18.53	0.1935	-20.79	0.6473
13	$\delta V_{\tau 3}$ (mV)	27.22	0.0136	26.82	0.2939	26.63	**1.994**
14	t_3 (ms)	0.7011	0.0035	0.8124	0.2339	1.077	0.6005
15	ϵ_3 (ms)	12.90	0.0204	12.35	0.1620	11.98	0.2704
16	g_{K} (mS cm^{-2})	6.901	0.0081	4.379	0.2335	3.046	0.0981
17	E_{K} (mV)	-99.99	0.0771	-113.9	**8.812**	-118.8	**7.529**
18	V_{t4} (mV)	-34.58	0.0069	-35.76	0.2745	-36.32	0.2053
19	δV_4 (mV)	22.17	0.0078	19.97	0.4515	14.85	0.5289
20	$\delta V_{\tau 4}$ (mV)	23.57	0.0102	22.20	0.3481	18.77	0.2407
21	t_4 (ms)	1.291	0.0081	1.038	0.2834	0.7844	0.1177
22	ϵ_4 (ms)	4.315	0.0039	4.797	0.1185	7.165	0.1520
23	g_{H} (mS cm^{-2})	0.1500	0.0190	0.1499	**1.1751**	0.1396	**2.080**
24	E_{H} (mV)	-42.991	0.1401	-41.29	**1.049**	-34.33	**8.490**
25	V_{t5} (mV)	-76.012	0.0227	-75.89	0.6289	-75.96	1.735
26	δV_5 (mV)	-5.517	0.0531	-6.923	**1.006**	-9.162	**3.374**
27	$\delta V_{\tau 5}$ (mV)	20.278	0.2831	36.27	*16.92*	55.35	*30.57*
28	t_5 (ms)	6.445	0.7780	4.107	*43.81*	4.742	*38.13*
29	ϵ_5 (ms)	54.85	0.7259	51.77	**3.333**	48.21	**5.084**
30	$\bar{p}$ (μm s^{-1})	0.1035	0.4509	0.2065	*36.04*	0.0330	*4.068*
31	V_{t6} (mV)	-65.50	0.0191	-65.42	**2.098**	-63.48	*16.48*
32	δV_6 (mV)	12.40	0.0242	13.59	**3.394**	15.58	**8.806**
33	$\delta V_{\tau 6}$ (mV)	27.04	0.1222	19.25	**9.183**	13.49	*10.42*
34	t_6 (ms)	0.7318	0.5071	2.126	*35.76*	4.318	*46.99*
35	ϵ_6 (ms)	13.037	0.0509	27.97	*32.26*	51.12	*42.38*
36	V_{t7} (mV)	-86.00	0.2198	-80.91	**9.23**	-76.49	**4.69**
37	δV_7 (mV)	-8.061	0.0316	-4.811	**3.24**	-1.995	**2.56**
38	$\delta V_{\tau 7}$ (mV)	16.72	0.1425	14.59	**4.77**	22.82	**1.97**
39	t_7 (ms)	28.11	0.27	32.18	**8.497**	34.79	*17.59*
40	ϵ_7 (ms)	288.1	0.5512	358.8	*30.43*	287.2	*36.73*

parameters. Their standard deviations jump by an order of magnitude from RVLM to ErrM1 (Table II) and by a smaller increment from ErrM1 to ErrM2. Gate recovery times previously identified as the least-well-constrained parameters such as t_5 and ϵ_5 or t_6 and ϵ_6 are the most sensitive to model error. The (t_6, ϵ_6) pair is an extreme example where standard deviations jump from (0.5%,0.05%) (RVLM) to (35%,32%) (ErrM1) and (47%,42%) ErrM2.

Parameter correlations are also evident in the finite off-diagonal components of the ErrM1 and ErrM2 covariance matrices (Fig. 3) compared to the RVLM covariance matrix which has none, except for t_5 (parameter 28). The eigenvalues of the RVLM covariance matrix [Fig. 3(a)] are vanishingly small. In contrast, the ErrM1 and ErrM2 covariances have six nonzero eigenvalues. These represent the lengths of the principal semiaxes of the data misfit ellipsoid. In other words, instead of having a well-defined global minimum as in the well-posed case, the cost function now has deep valleys along which parameter correlations occur. We anticipate this result will hold more generally whenever an erroneous nonlinear model is synchronized to time series data. The largest correlations are within the parameters
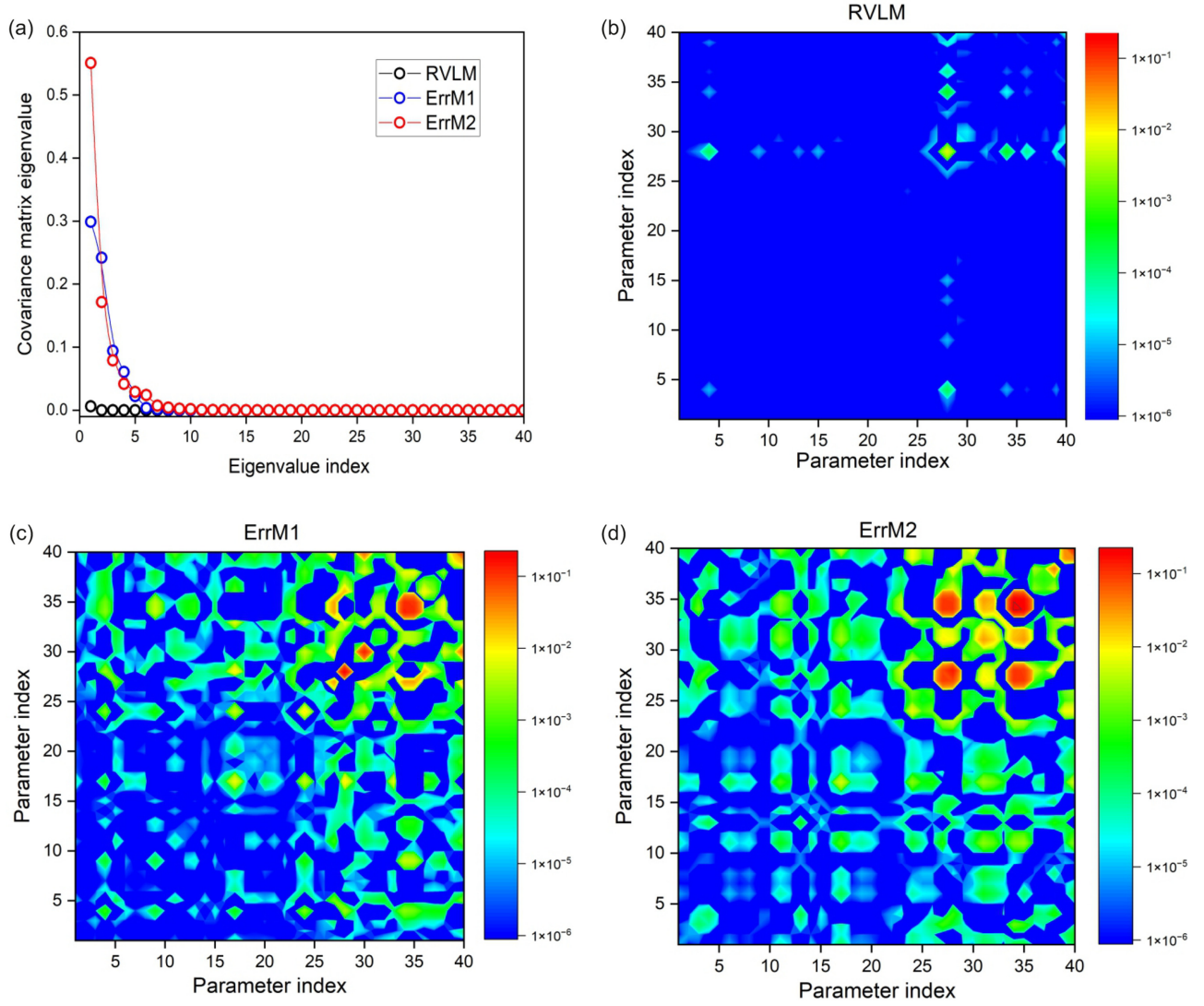
FIG. 3. Covariance maps of parameters inferred with the RVLM, ErrM1, and ErrM2 models. (a) Eigenvalues of the covariance matrix of parameters estimated with erroneous models ErrM1 (blue trace) and ErrM2 (red trace). The eigenvalues of the well-posed RVLM model (black trace) are shown for reference. Covariance maps of the (b) RVLM, (c) ErrM1, and (d) ErrM2 parameters.

of the CaT and HCN currents ($k > 25$) and they increase with increasing model error [Figs. 3(b)–3(d)]. An important point to note is the clustering of off-diagonal terms in blocks linking the parameters of individual ionic currents. This raises the prospect that parameter correlations may compensate each other in the calculation of ionic currents to

TABLE III. Na, K, and HCN ion discharge per action potential. The Q_{Na}, Q_K, and Q_{HCN} are the ionic volumes discharged during action potential (labeled with an asterisk in Fig. 2). The $\bar{Q}_1$ and Σ_1 are the mean values and standard deviations derived from a statistical sample of 41 ion current waveforms. These waveforms are predicted by 41 ErrM1 models completed with the 41 parameter sets from assimilation windows $\omega_1, \ldots, \omega_{41}$. The same was done for RVLM, ErrM2, ErrM3, and ErrM4. The $\bar{Q}_N$ and Σ_N are the mean charge and standard deviations obtained by assimilating noisy data with the RVLM model.

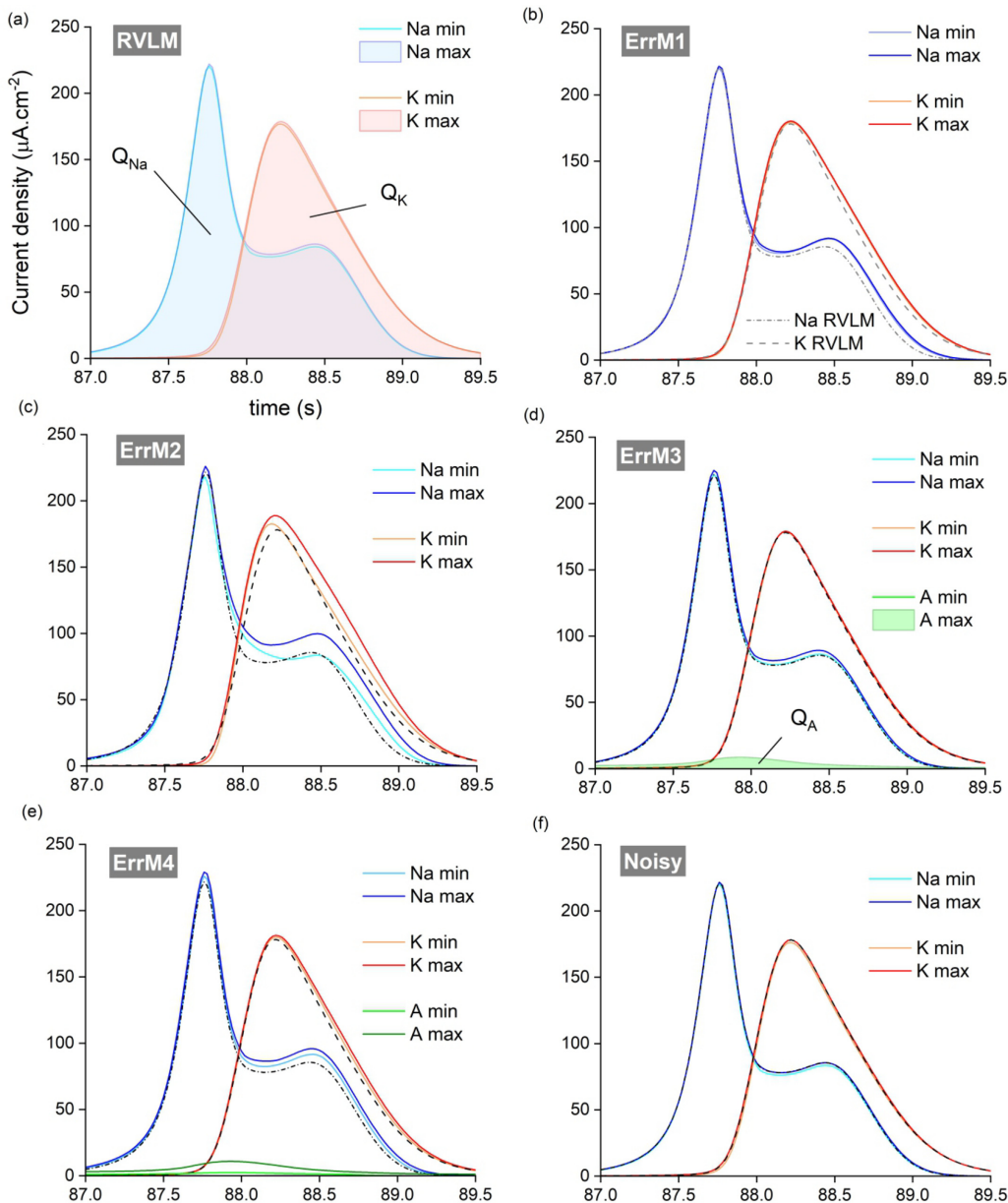|	Well-posed		Ill-posed									
	RVLM		ErrM1		ErrM2		ErrM3		ErrM4		Noisy	
Ionic volume (nC cm^{-2})	$\bar{Q}$ (%)	$\frac{\Sigma}{\bar{Q}}$ (%)	$\bar{Q}_1$ (%)	$\frac{\Sigma_1}{\bar{Q}_1}$ (%)	$\bar{Q}_2$ (%)	$\frac{\Sigma_2}{\bar{Q}_2}$ (%)	$\bar{Q}_3$ (%)	$\frac{\Sigma_3}{\bar{Q}_3}$ (%)	$\bar{Q}_4$ (%)	$\frac{\Sigma_4}{\bar{Q}_4}$ (%)	$\bar{Q}_N$ (%)	$\frac{\Sigma_N}{\bar{Q}_N}$ (%)
Q_{Na}	1126	**1.06**	1186	0.25	1224	**4.50**	1148	**1.48**	1166	**1.24**	1119	0.98
Q_K	1098	**1.54**	1147	0.26	1174	**3.32**	1113	0.45	1131	0.97	1091	**1.47**
Q_{HCN}	260	**3.46**	266	**2.69**	291	**4.85**	263	**2.28**	263	**1.90**	258	**3.49**

FIG. 4. Comparison of ionic currents predicted by erroneous and exact models. (a) Current waveforms predicted by the RVLM model. The minimum and maximum in the Na and K traces give the range of variation of currents reconstructed from the 41 assimilation windows. For reference, the true Na and K current waveforms predicted by the original RVLM model are shown as the black dashed lines in (b)–(f). Current waveforms are predicted by erroneous models (b) ErrM1; (c) ErrM2, an overspecified RVLM model; (d) ErrM3, an overspecified erroneous model; and (e) ErrM4 and from noisy data (f) Noisy.

make more accurate predictions than by relying on parameters alone.

Figure 4 shows the range of current waveforms reconstructed from our 41 sets of 40 parameters. For clarity, we only plot the minimum and maximum waveforms of this range. The minimum and maximum current waveforms predicted by the RVLM model are virtually identical to the original waveforms [Fig. 4(a)]. Quite remarkably, the ErrM1 model still predicts nearly identical minimum and maximum waveforms [Fig. 4(b)] despite the order of magnitude larger uncertainty in the underlying parameters (Table II). Only in the ErrM2 model does the dispersion in predicted currents become noticeable [Fig. 4(c)]. Note also the excellent agreement between the

currents predicted by ErrM1 and ErrM2 and the true RVLM current waveform (dashed lines). These results demonstrate that approximate models can still predict the true currents with a high degree of confidence despite large uncertainty in underlying parameters.

We then calculated the total Na and K charge transferred under the predicted current waveforms. The mean values $\bar{Q}$ and standard deviations Σ are given in Table III. The standard deviations $\Sigma_1/\bar{Q}_1$ (ErrM1) and $\Sigma_2/\bar{Q}_2$ (ErrM2) remain under 5% for all currents. This is considerably lower than the uncertainty on underlying parameters which can be as high as 50% (Table III). If we examine how close the average estimates are to true values we find that the $\bar{Q}_1$ is within 5% (Na) and

4% (K) of the original model prediction and $\bar{Q}_2$ is within 9% (Na) and 7% (K). The ionic charges predicted by erroneous models ErrM1 and ErrM2 are therefore an excellent predictor of the true ionic charges. In our example, decreasing the Na gate exponent effectively decreases the slope of the activation curve. Recursive piecewise data assimilation compensates for the subsequent widening of the activation curve by reducing the width parameter δV_2 from 10 (RVLM) to 8.1 (ErrM1) and 5.2 (ErrM2) in Table II. The large deviation (50%) of such a parameter from the true value is a second reason why ionic currents constitute more stable predictors of true values when the model is unknown.

2. Overspecified models: ErrM3 and ErrM4

It is sometimes argued that model overspecification causes multivalued solutions. We investigate this hypothesis by constructing two overspecified models, adding a supernumerary A-type current to the RVLM model (ErrM3) and to the ErrM1 model (ErrM4). The A-type current density is $J_A = g_A x_{14} x_{15} (x_1 - E_K)$, where x_{14} and x_{15} are the activation and inactivation variables, respectively, and E_K is the potassium reversal potential.

We find that the ErrM3 problem has a single-value solution that yields the true RVLM parameters. In the process, RPDA correctly filters out the A-type current by assigning a negligible value to g_A. The standard deviations of the ErrM3 parameters are also small (less than 0.01%) and comparable to those of the RVLM model (Table II). The narrow dispersion of parameter estimates explains the narrow dispersion of the predicted current waveforms and their similarity to the true current waveforms [dashed lines in Fig. 4(d)]. The mean ion volume discharged per action potential, $\bar{Q}_3$, is within 1.5% (Na) and 3% (K) of true values and hence is also an excellent predictor of true ion discharge. The standard deviations Σ_3 are similar to those of the RVLM model (Table III). These results show that model optimization successfully disentangles the contributions of individual ion channels to the membrane voltage based of the characteristic mathematical form of each ionic current [Eqs. (A2) and (B2)], which act like a fingerprint. This allows RPDA to prune out the extra A current even if *a priori* the identifiability criterion is broken by model overspecification.

Now turning to the ErrM4 model, one might argue that large models succeed in inferring the correct parameters and currents because it is the exact (RVLM) model that one overspecifies. One hypothesis is that if the A channel was added to a wrong model such as ErrM1, its parameters might compensate for the erroneous Na gate exponent. Examination of parameter distributions show nothing of the sort occurs. Recursive piecewise data assimilation assigns a vanishing conductance g_A to the supernumerary "A channel." This can be seen in Fig. 4(e), where the A current is zero within a standard deviation. The predicted Na and K current waveforms remains in excellent agreement with true waveforms (dashed lines) and carry a high degree of confidence *in spite of model error*. Turning to the mean charge transferred per action potential, $\bar{Q}_4$, we find ErrM4 predicts the true ionic discharge within 3.5% (Na) and 3% (K) of true values. The volume of A-type charge transfer, $\bar{Q}_4 = 82$ nC cm^{-2}, remains

tiny compared to 1166 nC cm^{-2} for Na and 1131 nC cm^{-2} for K, indicating the A channel does not compensate for gate exponent error. The standard deviations on discharged ions, Σ_4, are small and comparable to those of the RVLM model (Table III).

These remarkable results indicate that RPDA successfully disentangles the contributions of all ion current types *even with approximate models that may include redundant ion channels*. Naturally, we have restricted our study to mild model error. It is evident that increasing the degree of model error by altering the equations of several ionic currents at the same time would eventually degrade the ability of RPDA to disentangle individual ion currents.

3. Data error: Assimilating noisy RVLM data

For completeness, we examine the case where the V_{mem} time series in Fig. 2(a) is corrupted by additive Gaussian noise. The noise rms amplitude of 0.1 mV is comparable to the noise level in patch-clamp recordings. Figure 4(f) shows the Na and K currents predicted by the RVLM model in this case. The current waveforms have a very narrow dispersion and are virtually identical to the true waveforms (dashed lines). Hence the impact of data error on predicted quantities will often be small compared to model error. The implications of noisy data in data assimilation were further discussed by Taylor *et al.* [65]. Nowadays, current-clamp recordings are of such high quality that noise and data error are rarely an issue. The real challenge is model error.

4. Unknown model: Hippocampal CA1 neuron

We complete our study of model error by investigating the distribution of parameters and ionic currents estimated using a guessed neuron model. Model error is now unknown, which means that the mean parameter and current estimates can no longer be compared to the biological values which we are seeking. We used the model to assimilate the current-clamp recordings of a hippocampal CA1 neuron [Fig. 5(a)]. We refer the reader to the work of Abu-Hassan *et al.* [71] for details on the experimental protocol. The guessed CA1 model had 9 ion channels and 70 parameters (see Appendix B). It includes the NaT, NaP, K, A-type, Ca, BK, SK, HCN, and leak ion channels believed to be present in the CA1 soma [72–74]. We obtained 71 sets of 70 parameters from sliding time windows. Each window was 200 ms long. Consecutive windows were offset by 2 ms, the same as in Fig. 2. The CA1 models completed with any of the 71 sets of parameters successfully predicted the observed membrane voltage [red trace in Fig. 5(a)]. The good predictive power of the completed models therefore suggests that the error in the model equations is mild.

From these 71 sets of parameters, we reconstructed the ionic current waveforms at the site of the action potential labeled by an asterisk in Fig. 5(a). The predicted sodium currents (NaP and NaT) and potassium currents (K, A, SK, and BK) are combined into Na and K waveforms in Fig. 5(b). While the waveform shapes are similar to those of our earlier models (Fig. 4), the predictions cover a wider range and the potassium current has a slower rate of decay [Fig. 5(b)]. The standard deviations on the ionic charge transferred per
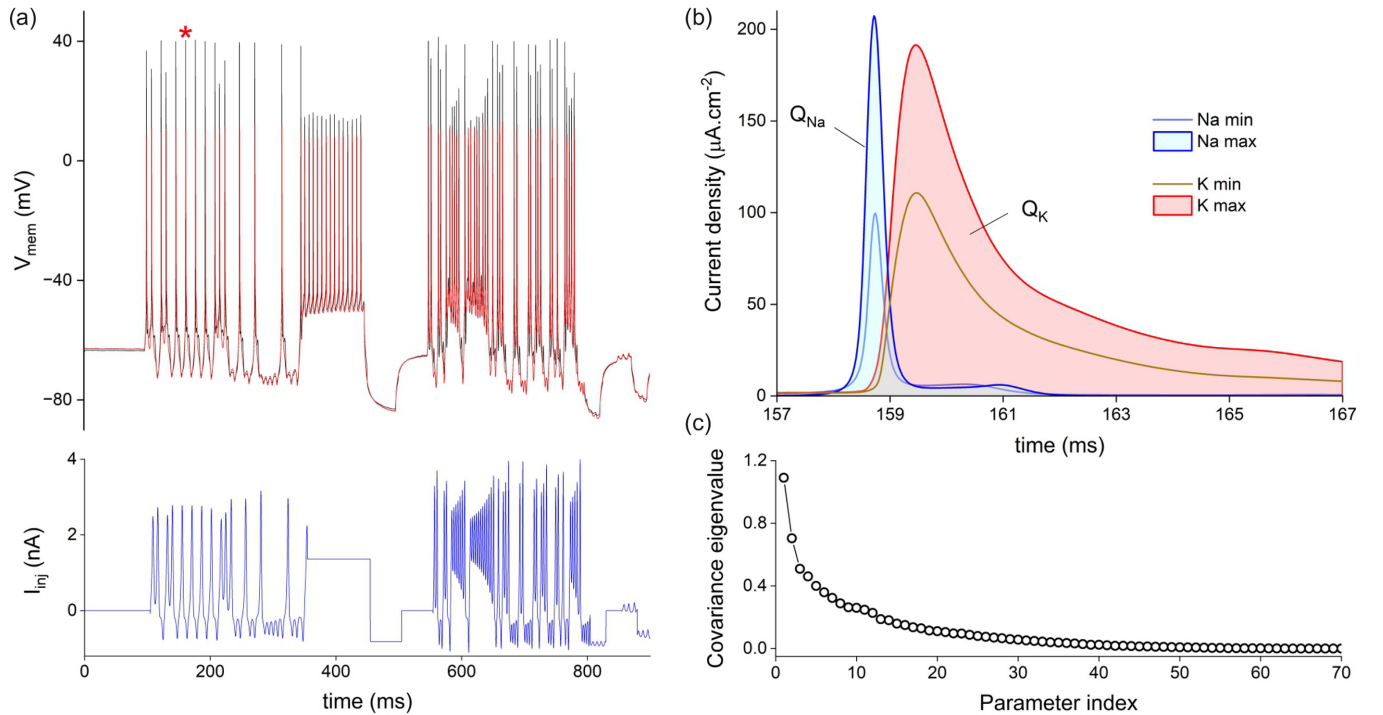
FIG. 5. Uncertainty on currents and parameters estimated from a hippocampal CA1 neuron. (a) Membrane voltage oscillations (black trace) driven by injecting a calibrated current waveform (blue trace) into a hippocampal neuron (Wistar rat, CA1 neuron). Voltage oscillations were predicted by the hippocampal neuron model completed with one set of parameters. The asterisk labels the action potential whose ionic current waveforms we predict in (b). (b) Minimum and maximum current waveforms (Na and K) predicted by 71 CA1 models completed with the parameters from 71 assimilation windows. (c) Eigenvalues of the 70×70 covariance matrix of estimated parameters.

action potential are 14.4% (Na) and 14.6% (K) (Table IV). These are 7 times larger than in the ErrM2 model, suggesting that the discrepancy between the guessed CA1 model and the actual CA1 neuron is approximately 7 times greater than the discrepancy between the ErrM2 model and the RVLM model. Another measure of model error is the eigenvalues of the parameter covariance matrix [Fig. 5(c)]. Although the CA1, ErrM1, and ErrM2 eigenvalues fall in the same range [Figs. 3(b), 3(c), and 5(c)], the CA1 distribution has a fatter tail of eigenvalues, which suggests the CA1 model has more parameters with small functional overlap.

IV. DISCUSSION

In well-posed problems, the RPDA method achieves a remarkable 100% convergence rate from 28 different initial conditions (Table I) and with 41 current waveforms (Table II). Improvement over the 64% convergence rate reported by

TABLE IV. Na and K ion discharge per action potential of a CA1 neuron. Mean ion volumes discharged Q and standard deviation Σ are at the action potential in Fig. 5 (denoted by an asterisk therein).

Ion discharge	CA1 neuron	
(nC cm^{-2})	$\bar{Q}$	$\frac{\Sigma}{\bar{Q}}$ (%)
Q_{Na}	73.43	14.4
Q_K	466.2	14.6

Taylor *et al.* [65] is achieved by reinjecting data in piecewise intervals and by recursively restarting the parameter search from a larger piecewise interval if convergence fails. The well-posed case was used to validate the fulfillment of the identifiability and observability criteria when the true parameter solution was recovered, starting from different initial conditions and current waveforms. With the caveat that a solution to such an NP-hard inference problem is not known to exist in general, our empirical simulations suggest that in the special case of neuron-based conductance models the RPDA method obtains a solution for systems of up to at least 14 differential equations which describe most neuron types. The RVLM model is an exemplar in this regard because any ionic current which may be added will have a similar mathematical form including sigmoidal activation and first-order gate dynamics.

By intentionally introducing model error in well-posed data assimilation (ErrM1 and ErrM2), multivalued solutions were found to occur due to correlations between parameters (Fig. 3). Averaging the parameters estimated from sliding assimilation windows gave mean parameter estimates within 15% of true values except for gate activation times, which deviated by a factor of 2 or more and had large uncertainty (up to 46%). In order to achieve a greater consistency in predictions, we calculated the ionic currents which integrate parameter correlations (Fig. 4). The mean ionic charge transferred per action potential deviated by less than 5% (ErrM1) and 8% (ErrM2) from true values and the coefficients of variation were very low at 0.26% (ErrM1) and 4.5% (ErrM2). It is

therefore anticipated that ionic currents could be predicted with sufficient accuracy to resolve changes in individual ionic currents induced by inhibitory drugs or ion channel dysfunction as done by Morris *et al.* [59]. The RPDA method could thus be incorporated in the drug screening pipeline as an effective drug toxicity counterscreen detecting changes and compensation mechanisms in ionic conduction occurring across the complement of ion channels. These are currently difficult to resolve with voltage clamps that analyze one ion channel at a time.

Overspecifying conductance models (ErrM3 and ErrM4) is no impediment to recovering the true parameters. The mean current waveforms estimated by ErrM3 are identical to those of the RVLM model and their coefficient of variation are identical (less than 1.5%). The ErrM3 waveforms remain close to the true waveforms (dashed lines in Fig. 4) and their coefficient of variation is also small (less than 1.2%). The charge transferred under the ErrM4 waveforms was within 4% of true values and the uncertainty on predictions was less than 1.3%, despite model error and overspecification. This demonstrates the ability of the RPDA method to disentangle the correct contribution of each ion channel to the membrane voltage without the overspecified current compensating for model error. The implication is that a universal conductance model could infer accurate information on ion channels without requiring any prior assumption on which ion channel might be expressed. The approximate models on which our conclusions are based had small model error affecting one ionic current. It is evident that systems incorporating more severe model error would eventually fail to make sensible predictions when optimized. Identifying how much model error the RPDA method can tolerate before its predictions would fail is an interesting question for future study. Our findings also suggest that reductionist models that minimize the number of parameters may not be the best route to improve accuracy of parameter estimates. Instead, focus should be on mitigating model error.

We found that standard deviations on parameters (Table II) and current estimates (Tables III and IV) increase with increasing model error. Therefore, standard deviations provide a metric to quantify how close a guessed model is to the unknown biological model.

A possible strategy for correcting model error has been outlined by Abarbanel and co-workers [75,76]. This consists in adding a model error term to the cost function and balancing data error and model error in such a way as to eliminate the bias of model error on the parameter solution. When model error is properly weighted, parameters are assigned true values without having to compensate for model error. The outstanding challenge here is to determine the covariance matrix weighting the model error term. We have attempted to include a model error term in Eq. (3) by weighting it with a single hyperparameter as done by Ye *et al.* [75]. However, this approximation of the model error covariance matrix has proved too simplistic to resolve all constraint violations. The optimal value of such a hyperparameter was found to drift to zero or infinity during parameter search. Further progress will require novel methods to be developed to evaluate the covariance matrix weighting model error.

V. CONCLUSION

We have introduced recursive piecewise data assimilation as a novel method for optimizing neuron-based conductance models. Recursive piecewise data assimilation improves over earlier parameter estimation methods by biasing the parameter search with data and by iteratively improving the solution as the bias is gradually released. When the model is known, RPDA achieves a 100% convergence rate towards the true solution for a wide range of initial conditions and training data sets. When the model is unknown, model error introduces correlations between parameters estimates. The largest correlations occur between parameters that define each ionic current. By reconstructing the ionic currents, parameter correlations cancel out and the current waveforms are found to approximate very well the true current waveforms. The ionic charge transferred under these curves is also predicted with a high degree of confidence of 95.5% when model error affects a single ion channel and 85% when the true biological model is guessed (CA1 neuron). The increasing uncertainty of predictions with increasing model error suggests that the covariance matrix of parameters is a good metric of model error. We also found that model overspecification is not responsible for parameter sloppiness and that RPDA correctly disentangles all ion channel contributions to the membrane voltage data even when the model has a wrong gate exponent. Our work shows that combining variational inference with statistical analysis offers good prospects for extracting sensible biological information from data.

APPENDIX A: RVLM NEURON MODEL

Our model of the rostral ventrolateral medulla considers the soma as a single compartment [22,65] with five types of ionic currents: transient sodium (NaT), delayed-rectifier potassium (K), low-threshold calcium (CaT), hyperpolarization-activated cation (HCN), and a leakage current L. The model has seven state variables ($L = 7$) and 40 adjustable parameters ($K = 40$). The neuron membrane voltage x_1 varies as

$$C\frac{dx_1}{dt} = -J_{\mathrm{NaT}} - J_{\mathrm{K}} - J_{\mathrm{CaT}} - J_{\mathrm{HCN}} - J_L + \frac{I_{\mathrm{inj}}(t)}{A}, \quad \text{(A1)}$$

when driven by injected current I_{inj}. The A is the effective area of the soma. The ionic current densities are

$$J_{\mathrm{NaT}} = g_{\mathrm{NaT}}x_2^3 x_3(x_1 - E_{\mathrm{Na}}),$$

$$J_{\mathrm{K}} = g_{\mathrm{K}}x_4^4(x_1 - E_{\mathrm{K}}),$$

$$J_{\mathrm{HCN}} = g_{\mathrm{H}}x_5(x_1 - E_{\mathrm{H}}),$$

$$J_{\mathrm{CaT}} = 4\bar{p}x_6^2 x_7 \frac{x_1 F^2}{RT}\frac{[\mathrm{Ca}^{2+}]_i - [\mathrm{Ca}^{2+}]_o e^{-2Fx_1/RT}}{1 - e^{-2Fx_1/RT}},$$

$$J_L = g_L(x_1 - E_L). \quad \text{(A2)}$$

Nominal values of reversal potentials are $E_{\text{Na}} = +41$ mV, $E_{\text{K}} = -100$ mV, $E_{\text{H}} = -43$ mV, and $E_L = -65$ mV; ionic conductances $g_{\text{NaT}} = 69.0$ mS cm^{-2}, $g_{\text{K}} = 6.90$ mS cm^{-2}, $g_{\text{H}} = 0.15$ mS cm^{-2}, and $g_L = 0.465$ mS cm^{-2}; maximum calcium permittivity $\bar{p} = 0.103$ μm s^{-1}; and intracellular and extracellular calcium concentrations $[\text{Ca}^{2+}]_i = 2.4 \times 10^{-10}$ mol cm^{-3} and $[\text{Ca}^{2+}]_o = 2.0 \times 10^{-10}$ mol cm^{-6}. Here $F = 9.65 \times 10^4$ C mol^{-1} is Faraday's constant, $R = 8.324$ J K^{-1} mol^{-1} is the ideal gas constant, and $T = 298$ K.

Ionic gates follow a first-order dynamics

$$\frac{dx_l}{dt} = \frac{x_{l,\infty}(x_1) - x_l}{\tau_l(x_1)}, \quad l = 2, \dots, 7, \tag{A3}$$

where $x_l \in \{V, m, h, n, z, q, r\}$,

$$x_{l,\infty}(x_1) = \frac{1}{2}\left(1 + \tanh \frac{x_1 - V_{t,l}}{\delta V_l}\right),$$

$$\tau_l(V) = t_l + \epsilon_l\left(1 - \tanh^2 \frac{x_1 - V_{t,l}}{\delta V_{\tau,l}}\right). \tag{A4}$$

The nominal RVLM parameters are listed in the "True" value column of Table I. Equation (A1)–(A4) were configured with these parameters to generate the membrane voltage data V_{mem} in Fig. 2. The injected current waveform $I_{\text{inj}}(t)$ had 50 000 points with a 0.02-ms time step. The RVLM model was forward integrated with the odeint function of the SCIPY package in PYTHON 3. The resulting V_{mem} data were then assimilated by the RVLM system and its Errm1 to ErrM4 variants.

APPENDIX B: HIPPOCAMPAL NEURON MODEL

This hippocampal neuron model includes the ion channels in the soma of CA1 neurons [72–74,77,78]: persistent sodium current (NaP), an A-type potassium current (A), and calcium activated potassium currents (SK and BK) in addition to the NaT, K, calcium, HCN, and leak currents of the previous RVLM model. The model now has 9 ionic currents, 14 state variables ($L = 14$), and 69 adjustable parameters ($K = 69$). The membrane voltage dynamics is given by

$$C\frac{dx_1}{dt} = -J_{\text{NaT}} - J_{\text{NaP}} - J_{\text{K}} - J_{\text{A}} - J_{\text{Ca}}$$

$$- J_{\text{BK}} - J_{\text{SK}} - J_{\text{HCN}} - J_L + \frac{I_{\text{inj}}(t)}{A}. \tag{B1}$$

The ionic current densities are

$$J_{\text{NaT}} = g_{\text{NaT}}x_2 x_3^3 (x_1 - E_{\text{Na}}),$$

$$J_{\text{NaP}} = g_{\text{NaP}}x_4 (x_1 - E_{\text{Na}}),$$

$$J_{\text{K}} = g_{\text{K}}x_5^4 (x_1 - E_{\text{K}}),$$

$$J_{\text{A}} = g_{\text{A}}x_6 x_7 (x_1 - E_{\text{K}}),$$

$$J_{\text{Ca}} = g_{\text{Ca}}x_8^2 x_9 (x_1 - E_{\text{Ca}}),$$

$$J_{\text{BK}} = g_{\text{BK}}x_{10}^2 x_{11} (x_1 - E_{\text{K}}),$$

$$J_{\text{SK}} = g_{\text{SK}}x_{12} (x_1 - E_{\text{K}}),$$

$$J_{\text{HCN}} = g_{\text{H}}x_{13} (x_1 - E_{\text{HCN}}),$$

$$J_L = g_L (x_1 - E_L). \tag{B2}$$

The BK current depends on both the membrane voltage x_1 and the internal calcium concentration $[\text{Ca}^{2+}]_i \equiv x_{14}$, whereas the SK current depends on $[\text{Ca}^{2+}]_i$ only. The BK current has fast activation, which we take to be instantaneous in line with that of Warman et al. [72],

$$x_{10,\infty} = 0.5\left[1 + \tanh\left(x_1 - V_{10} + 130\frac{1 + \tanh\frac{x_{14}}{0.2} - 250}{\delta V_{10}}\right)\right], \tag{B3}$$

where the calcium equilibrium across the membrane is given by the rate equation

$$\frac{dx_{14}}{dt} = \frac{x_{14,\infty} - x_{14}}{\tau_{11}} - \frac{J_{\text{Ca}}}{4w}, \tag{B4}$$

driven by the calcium ion current J_{Ca}. The w is the thickness of the surface area across which Ca^{2+} fluxes are calculated ($w = 1$ μm). We modeled the dynamics of calcium gate variables x_8 and x_9 with Eqs. (A3) and (A4) with the appropriate calcium gate parameters.

The inactivation dynamics of the BK current has a long time constant τ_{11}. The rate equation

$$\frac{dx_{11}}{dt} = \frac{x_{11,\infty} - x_{11}}{\tau_{11}} \tag{B5}$$

also follows, where

$$x_{11,\infty} = 0.5\left[1 + \tanh\left(x_1 - V_{11} + 130\frac{1 + \tanh\frac{x_{14}}{0.2} - 250}{\delta V_{11}}\right)\right]. \tag{B6}$$

The activation dynamics of the SK current is fast ($x_{12} \equiv x_{12,\infty}$), and similar to the BK channel, the activation of the SK channel is described by

$$x_{12,\infty} = 0.5\left(1 + \tanh \frac{x_{14} - x_{t,12}}{\delta x_{\tau,12}}\right). \tag{B7}$$

Gate variables x_2 (NaP channel) and x_6 and x_7 (A channel) follow the first-order response in Eqs. (A3) and (A4) with the appropriate NaP and A channel parameters.

APPENDIX C: RPDA CODE

The cost function in Eq. (1) and linear constraints in Eqs. (2) and (3) were differentiated symbolically using our custom-built PYTHON library PYDSI to generate the C++ code of the optimization problem. This code inputs four text files specifying the dynamical system of Eqs. (2) and (3), dys_syn.txt; the bounds of Eqs. (4) and (5), bounds.txt; the problem size N, the starting point in the data file, and the option of using an adaptive step size [65], problem_info.txt; and the initial size of the piecewise interval M_0 and the M_0 increment value, recursive_info.txt. This code was then inserted in the open-source IPOPT software [79] implementing the MA97 linear solver [80]. The optimizations were run on a 16-core (3.20-GHz) Linux workstation with 64 GB of RAM and a University of Bath minicomputer with 64 processors and

320 GB of RAM. Model equations (2) and (3) were linearized according to Simpson's rule and Hermite interpolation [Eq. (6)].

Experiments on rodents were performed under Schedule 1 in accordance with the United Kingdom Scientific procedures act of 1986.

[1] A. Wächter and L. T. Biegler, On the implementation of an interior-point filter line-search algorithm for large-scale nonlinear programming, Math. Program. **106**, 25 (2006).

[2] S. Boyd and L. Vandenberghe, *Convex Optimization* (Cambridge University Press, Cambridge, 2004).

[3] F. T. Bergmann, S. Sahle, and C. Zimmer, Piecewise parameter estimation for stochastic models in COPASI, Bioinformatics **32**, 1586 (2016).

[4] J. D. Hogg and J. A. Scott, HSL_MA97: A bit-compatible multifrontal code for sparse symmetric systems, Science and Technology Facilities Council, Report No. RAL-TR-2011-024, 2011 (unpublished).

[5] L. Petzold, Automatic selection of methods for solving stiff and nonstiff systems of ordinary differential equations, SIAM J. Sci. Stat. Comput. **4**, 136 (1983).

[6] H. W. Kuhn and A. W. Tucker, in *Proceedings of the Second Berkeley Symposium on Mathematical Statistics and Probability, Berkeley, 1950*, edited by J. Neyman (University of California Press, Berkeley, 1951), Vol. 2, pp. 481–492.

[7] E. Kalnay, *Atmospheric Modeling, Data Assimilation and Predictability* (Cambridge University Press, Cambridge, 2003).

[8] U. Parlitz, J. Schumann-Bischoff, and S. Luther, Quantifying uncertainty in state and parameter estimation, Phys. Rev. E **89**, 050902(R) (2014).

[9] A. Nogaret, C. D. Meliza, D. Margoliash, and H. D. I. Abarbanel, Automatic construction of predictive neuron models through large scale assimilation of electrophysiological data, Sci. Rep. **6**, 32749 (2016).

[10] C. D. Meliza, M. Kostuk, H. Huang, A. Nogaret, D. Margoliash, and H. D. I. Abarbanel, Estimating parameters and predicting membrane voltages with conductance-based neuron models, Biol. Cybern. **108**, 495 (2014).

[11] A. Nogaret, Approaches to parameter estimation from model neurons and biological neurons, Algorithms **15**, 168 (2022).

[12] H. D. I. Abarbanel, *Predicting the Future: Completing Models of Observed Complex Systems* (Springer, Berlin, 2013).

[13] E. Armstrong, Statistical data assimilation for estimating electrophysiology simultaneously with connectivity within a biological network, Phys. Rev. E **101**, 012415 (2020).

[14] G. Lillacci and M. Khammash, Parameter estimation and model selection in computational biology, PLoS Comput. Biol. **6**, e1000696 (2010).

[15] M. Pospischil, M. Toledo-Rodriguez, C. Monier, Z. Piwkowska, T. Bal, Y. Frégnac, H. Markram, and A. Destexhe, Minimal Hodgkin-Huxley type models for different classes of cortical and thalamic neurons, Biol. Cybern. **99**, 427 (2008).

[16] J. M. Bardsley, A. Solonen, H. Haario, and M. Laine, Randomize-then-optimize: A method for sampling from posterior distributions in nonlinear inverse problems, SIAM J. Sci. Comput. **36**, A1895 (2014).

[17] P. Achard and E. De Schutter, Complex parameter landscape for a complex neuron model, PLoS Comp. Biol. **2**, e94 (2006).

[18] P. Baldi, M. C. Vanier, and J. M. Bower, On the use of Bayesian methods for evaluating compartmental neural models, J. Comput. Neurosci. **5**, 285 (1998).

[19] T. Brookings, M. L. Goeritz, and E. Marder, Automatic parameter estimation of multicompartmental neuron models via minimization of trace error with control adjustment, J. Neurophysiol. **112**, 2332 (2014).

[20] D. A. McCormick and H. C. Pape, Properties of a hyperpolarization-activated cation current and its role in rhythmic oscillation in thalamic relay neurons, J. Physiol. Lond. **431**, 291 (1990).

[21] W. Gerstner and W. M. Kistler, *Spiking Neuron Models* (Cambridge University Press, Cambridge, 2002).

[22] D. J. A. Moraes, M. P. da Silva, L. G. H. Bonagamba, A. S. Mecawi, D. B. Zoccal, J. Antunes-Rodrigues, W. A. Varanda, and B. H. Machado, Electrophysiological properties of rostral ventrolateral medulla presympathetic neurons modulated by the respiratory network in rats, J. Neurosci. **33**, 19223 (2013).

[23] C. S. Chan, K. E. Glajch, T. S. Gertler, J. N. Guzman, J. N. Mercer, A. S. Lewis, A. B. Goldberg, T. Tkatch, R. Shigemoto, S. M. Fleming, D. M. Chetkovich, P. Osten, H. Kita, and J. D. Surmeier, HCN channelopathy in external globus pallidus neurons in models of Parkinson's disease, Nat. Neurosci. **14**, 85 (2011).

[24] M. Migliore and G. M. Shepherd, An integrated approach to classifying neuronal phenotypes, Nat. Rev. Neurosci. **6**, 810 (2005).

[25] B. J. Molyneaux, P. Arlotta, J. R. Menezes, and J. D. Macklis, Neuronal subtype classification in the cerebral cortex, Nat. Rev. Neurosci. **8**, 427 (2007).

[26] H. Zeng and J. R. Sanes, Neuronal cell-type classification: challenges opportunities and path forward, Nat. Rev. Neurosci. **18**, 530 (2017).

[27] B. Santoro, J. Y. Lee, D. J. Englot, S. Gildersleeve, R. A. Piskorowski, S. A. Siegelbaum, M. R. Winawer, and H. Blumenfeld, Increased seizure severity and seizure-related death in mice lacking HCN1 channels, Epilepsia **51**, 1624 (2010).

[28] H. Lerche, M. Shah, H. Beck, J. Noebels, D. Johnston, and A. Vincent, Ion channels in genetic and acquired forms of epilepsy, J. Physiol. **591**, 753 (2013).

[29] R. N. Gutenkunst, J. J. Waterfall, F. P. Casey, K. S. Brown, C. R. Myers, and J. P. Sethna, Universally sloppy parameter sensitivities in systems biology models, PLoS Comput. Biol. **3**, e189 (12007).

[30] T. O'Leary, A. C. Sutton, and E. Marder, Computational models in the age of large datasets, Curr. Opin. Neurobiol. **32**, 87 (2015).

[31] J. M. Goaillard, A. L. Taylor, D. J. Schulz, and E. Marder, Functional consequences of animal-to-animal variation in circuit parameters, Nat. Neurosci. **12**, 1424 (2009).

[32] A. A. Prinz, D. Bucher, and E. Marder, Similar network activity from disparate circuit parameters, Nat. Neurosci. **7**, 1345 (2004).

[33] F. Takens, in *Dynamical Systems and Turbulence, Warwick, 1980*, edited by D. Rand and L. S. Young, Lecture Notes in Mathematics Vol. 898 (Springer, Berlin, 1981), pp. 366–381.

[34] J. Schumann-Bischoff and U. Parlitz, State and parameter estimation using unconstrained optimization, Phys. Rev. E **84**, 056214 (2011).

[35] J. Schumann-Bischoff, S. Luther, and U. Parlitz, Estimability and dependency analysis of model parameters based on delay estimates, Phys. Rev. E **94**, 032221 (2016).

[36] D. Aeyels, Generic observability of differentiable systems, SIAM J. Control Optim. **19**, 595 (1981).

[37] D. Csercsik, K. M. Hangos, and G. Szederkényi, Identifiability analysis and parameter estimation of a single Hodgkin-Huxley type voltage dependent ion channel under voltage step measurement conditions, Neurocomputing **77**, 178 (2012).

[38] D. V. Raman, J. Anderson, and A. Papachristodoulou, Delineating parameter unidentifiabilities in complex models, Phys. Rev. E **95**, 032314 (2017).

[39] A. Raue, V. Becker, U. Klingmüller, and J. Timmer, Identifiability and observability analysis for experimental design in nonlinear dynamical models, Chaos **20**, 045105 (2010).

[40] U. Parlitz, J. Schumann-Bischoff, and S. Luther, Local observability of state variables and parameters in nonlinear modeling quantified by delay reconstruction, Chaos **24**, 024411 (2014).

[41] C. Letellier, L. Aguirre, and J. Maquet, How the choice of the observable may influence the analysis of nonlinear dynamical systems, Commun. Nonlinear Sci. **11**, 555 (2006).

[42] C. Letellier, L. A. Aguirre, and J. Maquet, Relation between observability and differential embeddings for nonlinear dynamics, Phys. Rev. E **71**, 066213 (2005).

[43] P. A. Getting, *in* Neuronal and Cellular Oscillators, *edited by J. W. Jacklet* (Dekker, New York, 1989), pp. 215–236.

[44] J. Jing and R. Gillette, Central pattern generator for escape mechanism in the notaspid sea slug: Pleurobranchea Californatica, J. Neurophysiol. **81**, 654 (1999).

[45] J. E. Rubin, N. A. Shevtsova, G. B. Ermentrout, J. C. Smith, and I. A. Rybak, Multiple rhythmic states in a model of the respiratory central pattern generator, J. Neurophysiol. **101**, 2146 (2009).

[46] E. Marder and D. Bucher, Central pattern generators and the control of rhythmic movements, Curr. Biol. **11**, R986(R) (2001).

[47] A. I. Selverston, Invertebrate central pattern generator circuits, Philos. Trans. R. Soc. B **365**, 2329 (2010).

[48] R. Clark, L. Fuller, J. A. Platt, and H. D. I. Abarbanel, Reduced-dimension, biophysical neuron models constructed from observed data, Neural Comput. **34**, 1545 (2022).

[49] A. G. Otopalik, A. G. Sutton, M. Banghart, and E. Marder, When complex neuronal structures may not matter, eLife **6**, e23508 (2017).

[50] H. Ori, E. Marder, and S. Marom, Cellular function given parametric variation in the Hodgkin and Huxley model of excitability, Proc. Natl. Acad. Sci. USA **115**, E8211 (2018).

[51] B. L. Kagan, Y. Hirakura, R. Azimov, R. Azimova, and M.-C. Lin, The channel hypothesis of Alzheimer's disease: Current status, Peptides **23**, 1311 (2002).

[52] J. Duda, C. Pötshke, and B. Liss, Converging roles of ion channels, calcium, metabolic stress, and activity pattern of *Substantia nigra* dopaminergic neurons in health and Parkinson's disease, J. Neurochem. **139**, 156 (2016).

[53] J. T. Brown, J. Chin, S. C. Leiser, M. N. Pangalos, and A. D. Randall, Altered intrinsic neuronal excitability and reduced Na$^+$ currents in a mouse model of Alzheimer's disease, Neurobiol. Aging **32**, 2109.e1 (2011).

[54] S. Chakroborty and G. E. Stutzmann, Calcium channelopathies and Alzheimer's disease: insight into therapeutic success and failure, Eur. J. Pharmacol. **739**, 83 (2014).

[55] C. A. Nurse, Neurotransmitter and neuromodulatory mechanisms at peripheral arterial chemoreceptors, Exp. Physiol. **95**, 657 (2010).

[56] J. K. Dreyer and J. Hounsgaard, Mathematical model of dopamine autoreceptors and uptake inhibitors and their influence on tonic and phasic dopamine signalling, J. Neurophysiol. **109**, 171 (2013).

[57] M. Oh, S. Zhao, and V. Matveev, Neuromodulatory changes in short-term synaptic dynamics may be mediated by two distinct mechanisms of presynaptic calcium entry, J. Comput. Neurosci. **33**, 573 (2012).

[58] F. Nadim and D. Bucher, Neuromodulation of neurons and synapses, Curr. Opin. Neurobiol. **29**, 48 (2014).

[59] P. G. Morris, J. D. Taylor, J. F. R. Paton, and A. Nogaret, Single-shot detection of alterations across multiple ionic currents from assimilation of cell membrane dynamics, Sci. Rep. **14**, 6031 (2024).

[60] A. L. Hodgkin and A. F. Huxley, A quantitative description of membrane current and its application to conduction and excitation nerve, J. Physiol. **117**, 500 (1952).

[61] A. N. Tikhonov, On the stability of inverse problems, Comptes Rendus (Doklady) de l' Academie des Sciences de l' URSS **39**, 176 (1943).

[62] H. D. I. Abarbanel, M. Kostuk, and W. Whartenby, Data assimilation with regularized nonlinear instabilities, Q. J. R. Meteorolog. Soc. **136**, 769 (2010).

[63] D. R. Creveling, P. E. Gill, and H. D. I. Abarbanel, State and parameter estimation in nonlinear systems as an optimal tracking problem, Phys. Lett. A **372**, 2640 (2008).

[64] D. Rey, M. Eldridge, U. Morone, H. D. I. Abarbanel, U. Parlitz, and J. Schumann-Bischoff, Using waveform information in nonlinear data assimilation, Phys. Rev. E **90**, 062916 (2014).

[65] J. D. Taylor, S. Winnall, and A. Nogaret, Estimation of neuron parameters from imperfect observations, PLoS Comput. Biol. **16**, e1008053 (2000).

[66] C. Zimmer and S. Sahle, Deterministic inference for stochastic systems using multiple shooting and a linear noise approximation for the transition probabilities, IET Syst. Biol. **9**, 181 (2015).

[67] *Advanced Data Assimilation for Geosciences*, edited by E. Blayo, M. Bocquet, E. Cosme, and L. F. Cugliandolo, Lecture Notes of the Les Houches School of Physics (Oxford University Press, Oxford, 2012).

[68] W. Soofi, M. L. Goeritz, T. J. Kispersky, A. A. Prinz, E. Marder, and S. Wolfgang, Phase maintenance in a rhythmic motor pattern during temperature changes *in vivo*, J. Neurophysiol. **111**, 2603 (2014).

[69] J. A. Haley, D. Hampton, and E. Marder, Two central pattern generators from the crab, *Cancer borealis*, respond robustly and differentially to extreme extracellular pH, eLife **7**, e41877 (2018).

[70] D. Hampton, S. Kedia, and E. Marder, Alterations in network robustness upon simultaneous temperature and pH perturbations, J. Neurophysiol. **131**, 509 (2024).

[71] K. Abu-Hassan, J. D. Taylor, P. G. Morris, E. Donati, Z. A. Bortolotto, G. Indiveri, J. F. R. Paton, and A. Nogaret, Optimal solid state neurons, Nat. Commun. **10**, 5309 (2019).

[72] E. N. Warman, D. M. Durand, and G. L. Yuen, Reconstruction of hippocampal CA1 pyramidal cell electrophysiology by computer simulation, J. Neurophysiol. **71**, 2033 (1994).

[73] R. D. Traub, R. K. Wong, and R. M. H. Michelson, A model of a CA3 hippocampal pyramidal neuron incorporating voltage-clamp data on intrinsic conductances, J. Neurophysiol. **66**, 635 (1991).

[74] H. Karst, M. Joels, and W. J. Wadman, Low-threshold calcium current in dendrites of the adult rat hippocampus, Neurosci. Lett. **164**, 154 (1993).

[75] J. Ye, D. Rey, N. Kadakia, M. Eldridge, U. I. Morone, P. Rozdeba, H. D. I. Abarbanel, and J. C. Quinn, Systematic variational method for statistical nonlinear state and parameter estimation, Phys. Rev. E **92**, 052901 (2015).

[76] H. D. I. Abarbanel, *The Statistical Physics of Data Assimilation and Machine Learning* (Cambridge University Press, Cambridge, 2022).

[77] D. Golomb, C. Yue, and Y. Taari, Contribution of persistent Na^+ current and M-type K^+ current to somatic bursting in CA1 pyramidal cells: combined experimental and modeling study, J. Neurophysiol. **96**, 1912 (2006).

[78] C. Yue, S. Remy, H. Su, H. Beck, and Y. Yaari, Proximal persistent Na^+ channels drive spike after-polarizations and associated bursting in adult CA1 pyramidal cells, J. Neurosci. **25**, 9704 (2005).

[79] https://coin-or.github.io/Ipopt/

[80] www.hsl.rl.ac.uk/catalogue